

Inter-Flake Quantum Transport of Electrons and Holes in Inkjet-Printed Graphene Devices


Feiran Wang, Jonathan H. Gosling, Gustavo F. Trindade, Graham A. Rance, Oleg Makarovskiy, Nathan D. Cottam, Zakhar Kudrynskiy, Alexander G. Balanov, Mark T. Greenaway, Ricky D. Wildman, Richard Hague, Christopher Tuck, T. Mark Fromhold, and Lyudmila Turyanska*

2D materials have unique structural and electronic properties with potential for transformative device applications. However, such devices are usually bespoke structures made by sequential deposition of exfoliated 2D layers. There is a need for scalable manufacturing techniques capable of producing high-quality large-area devices comprising multiple 2D materials. Additive manufacturing with inks containing 2D material flakes is a promising solution. Inkjet-printed devices incorporating 2D materials have been demonstrated, however there is a need for greater understanding of quantum transport phenomena as well as their structural properties. Experimental and theoretical studies of inkjet-printed graphene structures are presented. Detailed electrical and structural characterization is reported and explained by comparison with transport modeling that include inter-flake quantum tunneling transport and percolation dynamics. The results reveal that the electrical properties are strongly influenced by the flakes packing fraction and by complex meandering electron trajectories, which traverse several printed layers. Controlling these trajectories is essential for printing high-quality devices that exploit the properties of 2D materials. Inkjet-printed graphene is used to make a field effect transistor and Ohmic contacts on an InSe phototransistor. This is the first time that inkjet-printed graphene has successfully replaced single layer graphene as a contact material for 2D metal chalcogenides.

1. Introduction

The discovery and isolation of single layer graphene (SLG) has opened new regimes of fundamental science and enabled transformative change in the architectures and performance of electronic devices.^[1] Upscaling device processing and co-depositing large-area graphene with other materials remain key challenges. For example, although large-area graphene layers have been produced by chemical vapor deposition (CVD) and molecular beam epitaxy (MBE),^[2] their electronic properties (e.g., mobility and conductivity) are inferior to those measured for high-quality mechanically exfoliated SLG.^[3,4] Liquid exfoliation of 2D materials offers an alternative way to produce 2D materials,^[5,6] which can be formulated into inks for scalable deposition by additive manufacturing (AM)/3D printing (3DP) technologies.^[7] Using an AM deposition, graphene and graphene oxide layers have been successfully printed to form macroscopic 3D structures,^[8,9] as well as

Dr. F. Wang, J. H. Gosling, Dr. G. F. Trindade, Prof. R. D. Wildman, Prof. R. Hague, Prof. C. Tuck, Dr. L. Turyanska
Centre for Additive Manufacturing
Faculty of Engineering
University of Nottingham
Nottingham NG7 2RD, UK
E-mail: Lyudmila.Turyanska@nottingham.ac.uk

 The ORCID identification number(s) for the author(s) of this article can be found under <https://doi.org/10.1002/adfm.202007478>.

© 2020 The Authors. Published by Wiley-VCH GmbH. This is an open access article under the terms of the Creative Commons Attribution License, which permits use, distribution and reproduction in any medium, provided the original work is properly cited.

DOI: 10.1002/adfm.202007478

J. H. Gosling, Dr. O. Makarovskiy, N. D. Cottam, Dr. Z. Kudrynskiy, Prof. T. M. Fromhold
School of Physics and Astronomy
University of Nottingham
Nottingham NG7 2RD, UK
Dr. G. F. Trindade
School of Pharmacy
University of Nottingham, University Park
Nottingham NG7 2RD, UK
Dr. G. A. Rance
Nanoscale and Microscale Research Centre (nmRC)
University of Nottingham
Nottingham NG7 2RD, UK
Dr. A. G. Balanov, Dr. M. T. Greenaway
Department of Physics
Loughborough University
Loughborough LE11 3TU, UK

complex micron-sized geometries^[10] and 3D nanocomposites^[11] on various substrates, including flexible substrates.^[12,13] Of particular interest is the application of AM for graphene fabrication of functional heterostructures and electronic devices. Recently, a fully inkjet-printed field effect transistor (FET) was demonstrated with a graphene layer and a top gate of hexagonal boron nitride (hBN).^[8] This has initiated a new wave of research into 3D-printed 2D electronics for photon detectors,^[14] sensors,^[15] and capacitors^[16] for stretchable and wearable electronics.^[17,18] However, despite an expanding body of work, the properties of graphene inks are not yet fully understood, and their application potential is still poorly exploited. To accelerate the exploitation of these materials, a comprehensive understanding of the origin and characteristics of charge transport in a network of randomly deposited nanoscale 2D flakes or nanoparticles assembled into macroscopic 3D structures is required. Previously, the effect of layer thickness on the resistivity of printed graphene has been studied.^[8,19] This revealed a linear variation of current with printed layer thickness > 40 nm, as expected for 3D materials. The transport properties of other 3D printed graphene devices, such as graphene/hBN FETs,^[8] have also been analyzed by adapting an approach first developed for SLG devices,^[4] where the charge carrier concentration and field-effect mobility are determined from the gate voltage dependence of the conductivity.

Here, we report experimental and theoretical studies of electron transport in 3D-printed graphene and hBN/graphene structures, which elucidate the inter-flake electron and hole percolation dynamics across multiple printed layers and determine the macroscopic electrical properties. Our results show that controlling the inter-flake electron trajectories is vital for printing devices that exploit the unique characteristics of mechanically exfoliated 2D materials. We focus on devices produced by inkjet-printing graphene/polymer composite inks with different layer thicknesses. We investigate how the electrical conductivity depends on the thickness of the printed graphene layer and on the applied gate voltage. The electrical properties of these layers are explained by developing an inter-flake quantum transport model that includes both semi-classical percolation transport^[20,21] and quantum tunneling between graphene sheets.^[4] Structural and compositional properties of graphene are probed

by TOF SIMS revealing some structural non-uniformity. To explain the dependence of conductivity on layer thickness we develop a Monte Carlo model for electron transport in inkjet-printed random graphene networks. Crucially, our analysis reveals the role of extended electron trajectories, which meander between flakes, and determine the device characteristics. We also demonstrate, for the first time, that inkjet-printed graphene can successfully replace single layer graphene as a contact material for 2D metal chalcogenides (e.g., InSe) to form Ohmic contacts. Finally, we report an example application of inkjet-printed graphene as an active channel in a fully 3D printed FET. Our results provide new insights into electron transport in 3D-printed heterostructures based on 2D materials, which could inform strategies for their implementation in future generations of additively manufactured device architectures.

2. Results and Discussion

2.1. Properties of Printed Graphene Layers

Graphene inks, containing liquid exfoliated graphene flakes (average size of 2590 nm²) and ethyl cellulose (EC) dispersed in a mixture of cyclohexanone/terpineol, were deposited onto borosilicate glass or Si/SiO₂ substrates using a drop-on-demand (DoD) inkjet printer (**Figure 1a**). Following ink deposition, layers were annealed in a vacuum oven at 250 °C to remove the solvent and decompose the additives within the ink. Micro Raman spectroscopy was used to investigate the impact of annealing temperature, T_{ann} , on the quality of printed graphene samples. In all spectra, peaks were observed at 1350 cm⁻¹ (D band), 1580 cm⁻¹ (G-band), and 2700 cm⁻¹ (2D band),^[22] consistent with the presence of few-layer graphene in the printed layers (**Figure 1b**). The peak intensity ratios $I_{\text{D}}:I_{\text{G}}$ and $I_{2\text{D}}:I_{\text{G}}$ provide quantitative descriptors of number of structural defects (the extent of deviation of the crystalline arrangement from a perfect hexagonally organized planar network of carbon atoms) and the length scale of graphitic ordering (symptomatic of inter-layer organization), respectively.^[23–25] In the printed graphene sample prior to thermal annealing the ratios are $I_{\text{D}}:I_{\text{G}} < 0.5$ and $I_{2\text{D}}:I_{\text{G}} > 1.4$. As the annealing temperature increases, both ratios

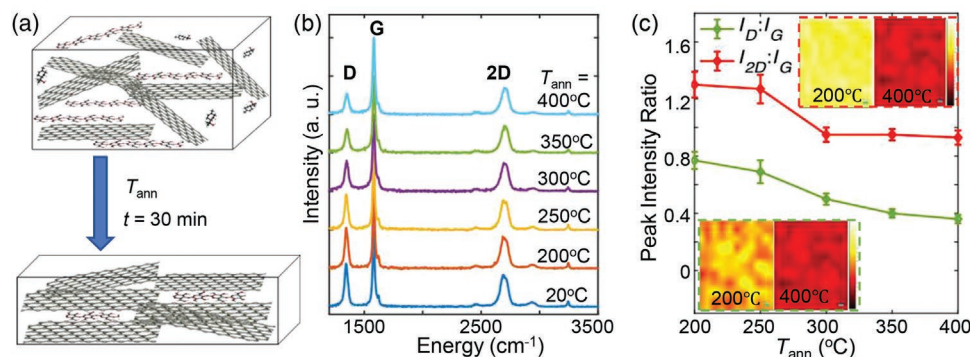


Figure 1. a) Schematic diagram of the inkjet-printed graphene-EC films showing graphene flakes and ink additives on the substrate before (top) and after (bottom) annealing at temperature T_{ann} . b) Raman spectroscopy of printed films (5 layers, sapphire substrate) annealed at different temperatures. Spectra have been normalized to the intensity of the G band and offset on the y -axis for visual clarity. c) Raman spectroscopy peak ratios $I_{\text{D}}:I_{\text{G}}$ and $I_{2\text{D}}:I_{\text{G}}$ measured for different annealing temperatures; insets show Raman mapping of the $I_{2\text{D}}:I_{\text{G}}$ (top inset) and $I_{\text{D}}:I_{\text{G}}$ (lower inset) peak ratios measured over a printed graphene area of 200 μm side-length for samples annealed at different annealing temperatures.

decrease and the 2D peak becomes broader and more symmetrical (Figure 1c), with the largest spectral changes observed for the sample annealed at 250 °C. This indicates that higher annealing temperatures reduce the defect density within a given graphitic lattice, but also decrease the interlayer organization, forming a more axially-disordered turbostratic graphite-like structure (Figure 1a), probably due to decomposition of ethyl cellulose at elevated temperatures above 250 °C.^[26,27] Raman mapping across 200 μm² regions of films annealed at different temperatures (insets in Figure 1c) confirms the uniformity of the graphene layer composition.

The width of the printed shape (nominally a rectangle) can be controlled by changing the drop spacing, time between drop deposition, number of lines and number of printed layers. This width is generally governed by the viscosity of the ink, wettability of the substrate, and volatility of the solvent. To enable printing of complex geometries needed for different devices, we examine the effect of the number of printed lines on the width of the print on different substrates. Figure 2a shows that the width of the line increases from 245 ± 15 μm for 1 layer to 288 ± 15 μm for 5 printed layers deposited on Si/SiO₂ (10 lines, drop spacing 20 μm, 30 s pause between drops). By increasing the number of printed lines to 60, the width of the rectangle was increased to 1872 μm for Si/SiO₂ substrate and to 1535 μm for glass.

The thermal gravimetric analysis (TGA) studies revealed that decomposition of the EC-graphene composite starts at $T_{\text{ann}} = 250$ °C, resulting in ≈10% mass loss (Figure 2b), which

is attributed to the initial decomposition of EC.^[28,29] Any carbon char resulting from EC during decomposition could connect neighboring graphene flakes,^[29] thereby providing an electrically conductive path. The composite lost up to 80% of its mass observed at $T_{\text{ann}} = 400$ °C. We note that the boiling points of the solvents are 219 °C for terpineol and 156 °C for cyclohexanone. Consequently, $T_{\text{ann}} = 250$ °C is expected to evaporate most of the solvent, leaving only solvent residues adsorbed on the flakes.^[30]

The printing and post deposition processes affect the electrical properties of the graphene layers. The sheet resistance, R_s , decreases with increasing number of printed layers (Figure 2a) and is approximately five times lower for a two-layer sample (27 Ω sq⁻¹) compared to a single printed layer (148 Ω sq⁻¹). We attribute this decrease of R_s to formation of a film, in which continuous graphene coverage is formed providing channels for charge transport. We note, that optical microscopy and SEM images of the sample with two- or more layers reveal a uniform film with no visible defects (see, e.g., inset in Figure 2b). The increase in the number of printed layers results in increasing thickness of the sample, and we observe saturation of the resistivity change for samples with more than two layers (see Section S1, Supporting Information), as expected for nano-networks.^[31] The value of T_{ann} also affects the R_s . We observe a significant decrease in the sheet resistance of layers annealed at $T_{\text{ann}} = 250$ °C, followed by a smaller decrease as T_{ann} is increased to 350 °C (Figure 2b). Increasing T_{ann} above 350 °C does not lead to further decrease of resistance. Our samples have lower resistivity than those reported in the literature, for example

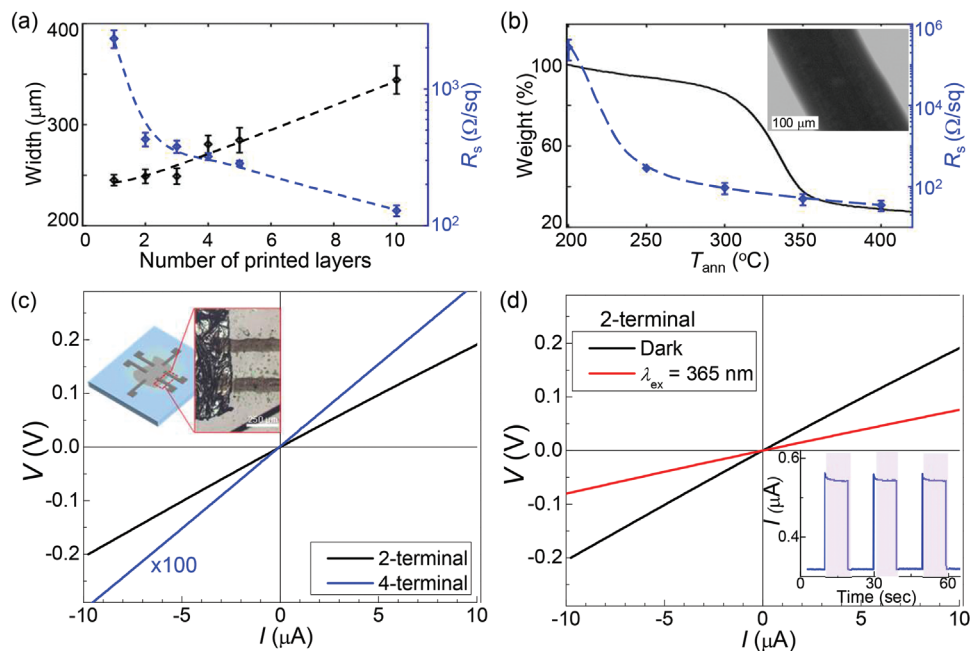


Figure 2. a) Printed line width and sheet resistance measured versus the number of inkjet-printed layers of graphene (10 lines, $T_{\text{ann}} = 250$ °C). b) Thermal gravimetric analysis (TGA) of the ink and corresponding sheet resistance measured versus annealing temperature (5 layers/10 lines). (Inset) The scanning electron microscopy image of graphene sample (5 layers/6 lines on Si/SiO₂, $T_{\text{ann}} = 250$ °C). c) Representative two-terminal and four-terminal current–voltage, I - V , characteristic measured for the InSe phototransistor at $T = 300$ K in the dark. (Inset) Schematic representation and an optical microscopy image of the structure of a phototransistor consisting of an exfoliated InSe flake contacted with six inkjet-printed graphene stripes (each comprising 5 printed layers, 7 lines), which serve as electrodes, on a 300 nm SiO₂/Si substrate. d) Representative current–voltage, I - V , characteristic measured for the InSe phototransistor at $T = 300$ K in the dark and under UV excitation. (Inset) the photocurrent measured under unfocused excitation with $\lambda_{\text{ex}} = 365$ nm.

for 5-layer samples annealed at $T_{\text{ann}} = 250$ °C we achieve the value of $\rho \approx 2 \times 10^{-5}$ Ωm , compared to $\rho \approx 1.2 \times 10^{-6}$ [8] and $\rho \approx 4.5 \times 10^{-5}$ Ωm .^[32] The lower value of resistivity in our work can be attributed to annealing in vacuum (rather than blade coated and annealed in air), which suggests that higher conductivity can be achieved by eliminating oxidation. It has been proposed that charge transport in these films is governed by π - π stacking between aromatic residues of cellulose decomposition and the graphene.^[32]

Based on the results of micro-Raman spectroscopy and electrical characterization, we ascribe the decreasing R_s with increasing T_{ann} to the reduction of in-plane defects and decreased flake-to-flake layer separation. Hence, five printed layers and $T_{\text{ann}} = 250$ °C were chosen as the optimal printing parameters for further studies. Thermal treatment at temperatures ≤ 300 °C is also beneficial for achieving higher intra-layer ordering and for retaining few-layer graphene assemblies within the printed film. We also note that EC-hBN ink has similar rheology (surface tension of 32.7 mN m^{-1} and viscosity of 11.9 mPa s at room temperature) to that of graphene ink. Consequently, the same printing strategy was adopted for the high precision deposition of insulating hBN layers (≈ 15 μm wide using a 20 μm drop spacing) with sheet resistance, $R_s > 100$ M Ω sq^{-1} for a single printed layer.

To examine the practicality of the printed graphene structures for device applications, we fabricated a prototype phototransistor by inkjet-printing graphene electrodes on a thin indium selenide (InSe) van der Waals (vdW) semiconducting crystal. Conventional metal contacts (e.g., Au, Cr, Ti) on 2D vdW semiconductors often form high Schottky barriers for charge carrier transport across the interfaces, which causes large contact resistance,^[33,34] thus limiting device performance. Recently, exfoliated graphene was proven to make excellent Ohmic contacts to 2D InSe,^[35,36] but fabricating these contacts remains challenging. In our device, an exfoliated millimeter sized InSe flake deposited on Si/SiO₂ (300 nm SiO₂) was electrically contacted with inkjet-printed graphene in a Hall bar geometry (inset in Figure 2c). Each electrode has an $\approx 400 \times \approx 200$ μm overlap area with the InSe surface. Two-terminal and four-terminal measurements reveal linear and symmetrical I - V characteristics for all combinations of the contacts, indicating that printed graphene forms Ohmic contacts to InSe (Figure 2c), due to the favorable band alignment of InSe with graphene.^[37] We estimate the in-plane resistivity, $\rho_{\perp\text{C}}$, of the InSe-phototransistor to be ≈ 18 Ω cm, which is comparable to that measured with exfoliated graphene and other conventional contacts.^[37] Crucially, our device also retains the photosensitivity (Figure 2d), associated with InSe flakes.^[38] The observed UV photoresponsivity and response time are $R > 10^3$ A W^{-1} and $\tau < 50$ ms, respectively, which are comparable to previously reported values measured for InSe flakes with exfoliated graphene in visible range.^[37]

2.2. Monte Carlo Modeling of Charge Transport in 2D Networks

In order to control and optimize the properties of inkjet-printed graphene for enhanced device performance, comprehensive understanding of charge transport in this complex material is

required. To help achieve this, we model the conductive characteristics of the network of flakes by first using Monte Carlo simulation of the flake positions and then analyzing the percolation networks between flakes, including flake to flake charge transfer between two or several flakes. In this simulation we do not directly discriminate between quantum tunneling and hopping, which was suggested for graphene and graphene oxide networks.^[39–41] We consider a distribution of parallel flakes, each of volume $V_f = 50 \times 50 \times 1.95$ nm^3 consistent with the inks used. We define the packing fraction, $\text{PF} = V_{\text{gr}}/V_d$, as the ratio of the total volume occupied by graphene flakes, $V_{\text{gr}} = NV_f$, where N is the number of flakes, to the total device volume is $V_d = A_c L$, where A_c is the cross-sectional area and L is the channel length (Figure 3a).

To build the distribution of flakes, we start with a perfectly ordered and close-packed arrangement of flakes where the center of each flake has a fixed separation, $\langle d \rangle$, from that of its six neighbors in all directions, x , y , and z , and specify the number of distinct layers that the flakes occupy (Movie S1, Supporting Information). Next, we randomize both the overlap area between adjacent flakes on different planes and the distance between individual flakes, d , which is constrained to lie between 0 and $2\langle d \rangle$ (see also Section S2, Supporting Information). The PF can then be reduced by randomly removing flakes. Figure 3a shows a final configuration of flakes with a mean interlayer separation $\langle d \rangle = 0.85$ nm and $\text{PF} = 0.28$. The current, I , between flakes is assumed to depend exponentially on the distance, d , according to

$$I \propto AeV \exp(-\alpha(d + d_{\text{vdW}})) \quad (1)$$

where V is the potential difference between overlapping flakes on adjacent layers, A is the areal overlap of the flakes, α is the tunneling constant, and we offset the distance between flakes, d , by the van der Waals distance, $d_{\text{vdW}} = 0.335$ nm.^[42,43] We note, that the proportionality constant in Equation (1) could be temperature dependent hence representative of hopping transport. Equation (1) is derived using the Landauer–Büttiker formula^[44] with a tunneling probability found via the Wentzel–Kramers–Brillouin (WKB) approximation.^[45] This gives $\alpha = (2/\hbar) \sqrt{2m\phi_0}$, where ϕ_0 is the barrier height and m is the mass of the tunneling electron, which we assume to be the free electron mass. Taking $\phi_0 = 1$ eV, we find that Equation (1), which describes tunneling current between two individual flakes, explains well our experimental results. In particular, the calculated exponential dependence of conductivity on distance accurately describes measured dependence of resistance on layer thickness (Figure 3b) and gives a conductivity that agrees with the experimentally obtained value. The value of ϕ_0 used is comparable to that measured for tunneling between two graphene sheets,^[46,47] which gives a current–voltage relation with the same exponential dependence obtained from Equation (1) with $V \ll \phi_0$.^[43] Note that the approximation of a constant barrier height $\phi_0 \gg V$ is reasonable because the drain-source potential is ≤ 1 V, and the channel is made up of ≥ 100 flakes.

A current is driven through the simulated device by applying a voltage between the electrodes (Figure 3a) connected to the left- and right- most flakes. The potential of these “contact”

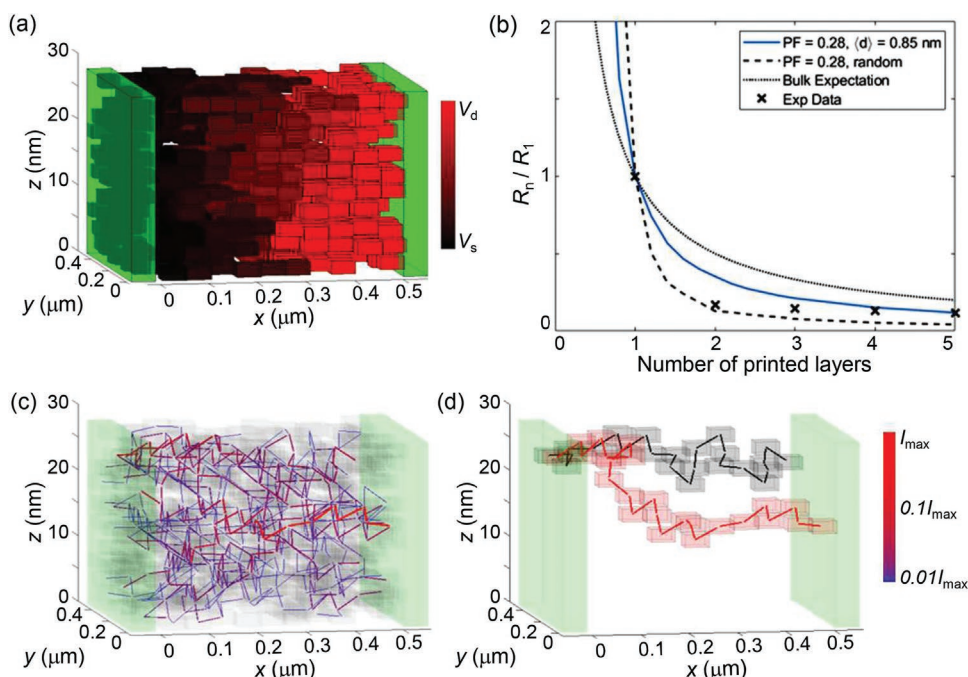


Figure 3. a) Representative arrangement of flakes used in our Monte Carlo simulation with packing fraction $PF = 0.28$ and mean interlayer separation $\langle d \rangle = 0.85$ nm, positioned between electrodes (green cuboids). The color of each flake represents the value of electrical potential (scale right). b) Ratio of electrical resistance, R_n , calculated for n printed layers to the resistance of one printed layer, R_1 for inkjet graphene with (blue curve) the flake arrangement shown in (a) and (black dashed curve) randomly distributed flakes. The expected dependence for a bulk conductor is shown by the solid black curve. The thickness of each layer is assumed to be 14 nm. Data points are our experimental results. The exponential dependence of conductivity on distance in Equation (1) accurately describes the measured dependence of resistance on layer thickness. c) Current paths between flakes (positions shown grey) with color-scaled current magnitudes (scale right). d) The two highest contributing current paths found following the path of highest current from left electrode to right (black) and vice versa (red).

flakes determines the boundary conditions, from which we calculate the potential of intermediate flakes self-consistently, by ensuring conservation of current through each flake.^[48,49] Note, that the resistance of each flake is neglected, since the tunneling resistance dominates (Section S2, Supporting Information). A hard-core/soft-shell model is adopted to define the range where flakes are considered adjacent:^[48,50] the hard-core is defined by the physical dimensions of the flakes and the soft-shell extends 2 nm beyond the hard-core. Any two flakes with overlapping shells are considered to be adjacent and thus form a junction for current flow. The 2 nm soft-shell allows for interflake distances up to 4 nm to contribute to the total current.

We set the constant of proportionality in Equation (1) so that for flakes in direct contact ($d = 0$) the conductivity is $\sigma_{\text{FLG}} = 40 \times 10^6 \text{ Sm}^{-1}$, comparable to that of few layer graphene (FLG).^[51] This value of σ_{FLG} is used as the highest possible value, that is, flakes in direct contact, hence we assume that the individual flakes have the conductivity of FLG and that contact resistance is negligible for flakes in direct contact. For $\langle d \rangle = 0.85$ nm and $PF = 0.28$, the conductivity is $\sigma = (1.01 \pm 0.32) \times 10^6 \text{ Sm}^{-1}$. The experimental values of conductivity are calculated using measured value of resistance, sample width and length (from optical microscopy) and the sample thickness value provided by ink manufacturer (14 nm per printed layer). We find that our theoretical estimate is in good agreement with the experimental value for two printed layer samples, where $\sigma = (1.3 \pm 0.4) \times 10^6 \text{ Sm}^{-1}$.

The resistance, R , of a bulk conductor is inversely proportional to its thickness. For our sample, the resistance decreases with increasing thickness (Figure 3b) but at a higher rate than that expected for bulk conducting material due to increased percolation arising from the randomized positioning of flakes. This percolation effect increases further when the positions of the flakes are completely randomized, rather than randomized about the mean separation $\langle d \rangle$. These results explain our experimental data (Figure 3b). The simulations reveal regions of inhomogeneity in the charge trajectories (Figure 3c) and potential landscape due to the randomized positioning of the flakes. As the thickness of the conductor decreases, the size of the regions of spatial inhomogeneity in the current become comparable to the device thickness, resulting in significant variance in the resistance between devices. Since the current between two flakes is determined by their areal overlap, the current between flakes which have a lateral overlap is significantly larger than the current between the edges of adjacent flakes. The two highest current percolation paths (Figure 3d), which meander between several layers, require tunneling in the z direction. Therefore, as the conductor thickness decreases, the probability of these high-conductivity meandering paths existing also decreases, thus increasing the resistance of the device. Our model reveals the mechanism of carrier transport in printed graphene layers and shows that optimized thickness of printed layers with high PF is required to achieve high conductivity devices.

2.3. Printed Graphene-Based Heterostructures for Functional Devices

In order to exploit printed graphene as active layers in a device, its performance in heterostructure devices needs to be assessed. Therefore, we fabricated a fully inkjet-printed FET with device geometry adapted from ref. [8]. Briefly, the device consists of a 100 μm wide (5 printed layers) graphene channel, source/drain contacts made from printed silver nanoparticles (AgNP) inks (resistivity $\approx 10 \mu\Omega \text{ cm}^{-1}$ [52]), and an $\approx 1.3 \mu\text{m}$ thick hBN/EC top gate dielectric layer. Inkjet-printed AgNP inks are used to deposit the electrical contacts.

The chemical composition of the FET was analyzed using scanning electron microscopy (SEM) and energy-dispersive X-ray spectroscopy (EDX) on a cross-section of the graphene/hBN/silver prints extracted from the channel region (Section S3, Supporting Information). The thickness of the hBN dielectric layer is $\approx 1.3 \mu\text{m}$ (50 printed layers) and the flakes are predominantly packed horizontally. The SEM image of the cross-section of the hBN/Ag/graphene heterostructure clearly revealed the hBN and silver layers. However, SEM identification of the graphene layer is challenging due to its low contrast and small thickness. We therefore employed time-of-flight secondary ion mass spectrometry (ToF-SIMS) to examine the morphology of the graphene layer. The C_6^+ signal was used to detect the presence of the graphene, where the ToF-SIMS 3D mapping of the device (Figure 4a) makes clear that the graphene layer thickness is not homogeneous over the $50 \times 50 \mu\text{m}^2$ area studied. The secondary ion profiles averaged over this area (Figure 4a) indicate that graphene flakes are present throughout an $\approx 300 \text{ nm}$ thick layer. However, the intensity of the C_6^+ signal is greatly reduced after $\approx 100 \text{ nm}$. These results indicate that there is an intermixing between consecutively deposited layers. For example, the top of the printed graphene layer is partially re-fluidized within the ink of the next deposited material. Hence, while graphene is present over an $\approx 300 \text{ nm}$ thick layer, the PF required for high conductivity is found only within a thinner ($\approx 100 \text{ nm}$) non-continuous region of this layer.

We now consider the electrical output and transfer characteristics of the graphene/hBN FET. For gate voltages of $V_g = -5, 0,$ and 5 V , the drain current increases linearly with V_{ds} (Figure 4b). The minima of the $I_{ds}(V_g)$ dependence occurs at low positive gate voltages, which indicates light p-doping of the graphene channel. Applying the analysis developed for single layer graphene, the carrier mobilities are calculated from $\mu = (L/W CV_{ds})/(dI_{ds}/dV_g)$, where L and W are the graphene channel length and width, respectively, and C is the dielectric capacitance.[4] Taking $L = 100 \mu\text{m}$, $W = 1000 \mu\text{m}$, and $C = 8.7 \text{ nFcm}^{-2}$,[8] we estimate the carrier mobilities to be $\mu_h = 22.9 \text{ cm}^2 \text{ V}^{-1} \text{ s}^{-1}$ and $\mu_e = 14.4 \text{ cm}^2 \text{ V}^{-1} \text{ s}^{-1}$. The difference between μ_h and μ_e is likely to originate from unintentional impurity doping, as reported previously for CVD and mechanically exfoliated graphene.[4]

The electrical resistance of the FET is higher than expected for 5-printed graphene layers because intermixing of the inks during layer-by-layer deposition, as evident from our ToF-SIMS results, reduces the effective thickness of the graphene layer with high PF. Due to the presence of high-resistance dielectric barriers between the graphene flakes (Figure 3), we can consider the flakes as conducting islands whose internal resistance is independent of V_g and lower than the inter-flake resistance. In addition, the relatively weak (compared to metals) electrical screening in undoped graphene[53] suggests that the vertical electric field produced by the applied V_g is homogeneous across the full thickness (i.e., $\approx 100 \text{ nm}$) of the conducting graphene channel. These assumptions allow us to simplify the model of charge carrier transport through the 3D-printed graphene network by introducing a statistically averaged flake-to-flake charge transfer process, which is independent of the positions of individual flakes determined from our Monte Carlo simulations. We adopt the activated conductivity theory[20,21] to explain the transport mechanism in the inkjet-printed graphene. We assume that charge transfer between graphene flakes, which act as discrete low-resistance islands, occurs via quantum mechanical tunneling, but that a finite activation (capacitive charging) energy, E_c , is required to place a single charge on a flake (Figure 5a). For $E_c > kT$,

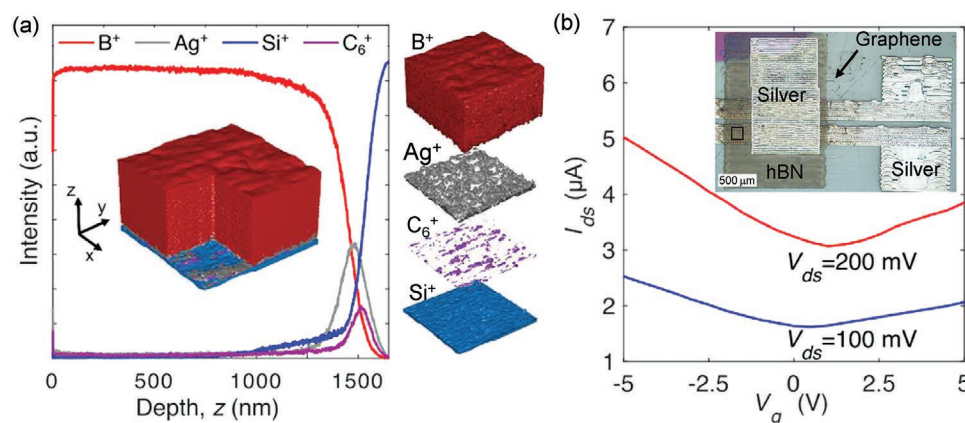


Figure 4. Characterization of the fully inkjet-printed graphene/hBN FET: a) Chemical composition determined by ToF-SIMS depth profiling and 3D mapping (inset and shown exploded on the right). b) Transfer characteristics measured for the graphene/FET when $V_{ds} = 100 \text{ mV}$ (blue curve) and 200 mV (red curve). Inset: Optical microscopy image of the graphene/hBN FET; scale bar is $500 \mu\text{m}$, spacing between silver electrodes is $100 \mu\text{m}$.

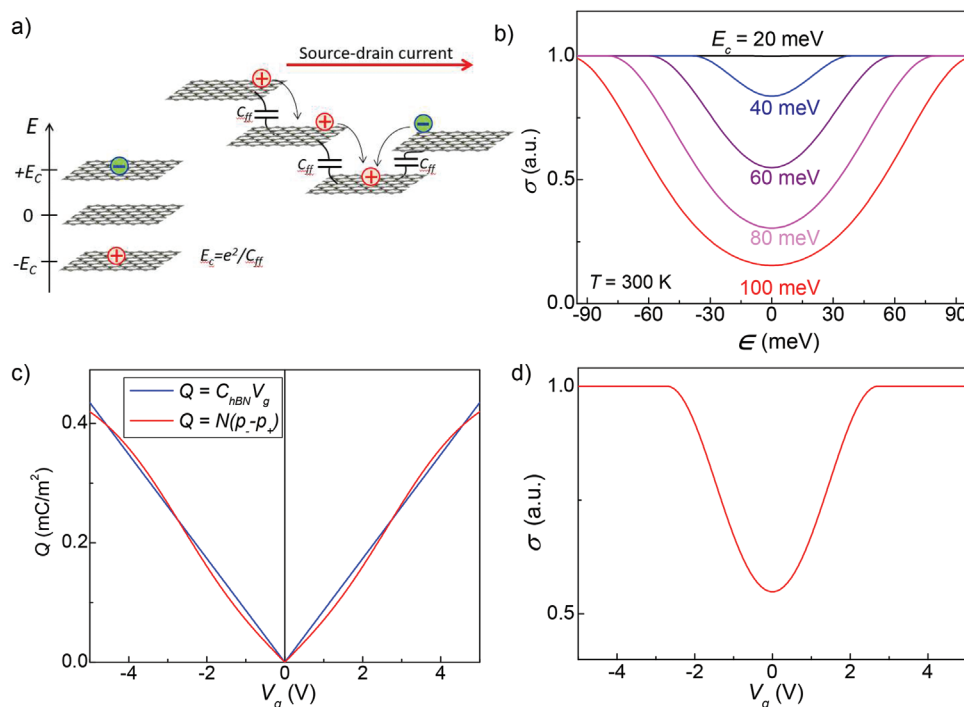


Figure 5. Charge transport model. a) Schematic of the capacitive charging process associated with inter-flake charge transfer. b) Conductivity calculated versus the excess energy, ϵ , for a range of different charging energies, E_c , (key inset) at $T = 300$ K. c) Total charge, Q , stored in the printed graphene layer calculated versus applied gate voltage, V_g , using a conventional parallel plate capacitance model (blue curve) and our inter-flake tunneling model (red curve). d) Conductivity, σ , calculated versus applied gate voltage, V_g , for the inter-flake tunneling model of charge transport in the 3D-printed graphene FET (cf. Figure 4).

we assume that only one positive or negative elementary charge can be present on each flake.^[8,54] Hence, the electrical conductivity can be calculated as (Sections S4,S5, Supporting Information)

$$\sigma \propto p_0 (p_- + p_+), \text{ where}$$

$$p_0 = \exp(E_c/kT) / [(\exp(E_c/kT) + 2 \cosh(\epsilon/kT))], \text{ and}$$

$$p_{\pm} = \exp(\mp \epsilon/kT) / [(\exp(E_c/kT) + 2 \cosh(\epsilon/kT))] \quad (2)$$

Here, p_0 , p_+ , and p_- are the probabilities of any one flake being neutral, positively, and negatively charged, respectively. We determine these probabilities using the standard Boltzmann distribution. The gate voltage modifies the charge density in the graphene channel, which is included in the model as the effective chemical potential, ϵ , of the charged island system. We determine the total charge on all of the flakes by using the constant capacitor charge balance equation^[21]

$$Q = C_g V_g = eN(p_- - p_+)A_f \quad (3)$$

where Q is the charge on the gate (or graphene) layer induced by applying a gate voltage V_g , where A_f is the flake area, N is the number of flakes per unit area, and C_g is the gate capacitance. Using $C_g = 8.7 \times 10^{-5} \text{ F m}^{-2}$,^[8] we estimate $\epsilon \approx 0.02eV_g$ (Figure 5c). We solve simultaneously Equations (2) and (3) to find the dependence of the conductivity on the thermal energy, kT , and gate voltage.

The charge concentration, n , and field effect mobility, μ_{FE} , can be deduced from the Drude conductivity model, $\sigma = en\mu_{FE}$, where, within the constant capacitance model, $n = eC_g V_g$. For the 3D printed graphene structures, n is a discrete function $n(V_g) = Q_d(V_g)/e$, where $Q_d(V_g)$ is the discrete charge per unit area, $Q_d = e \sum_{i=1}^N p_i$. The population, p_i , is equal to 1 or 0, depending on the presence or absence of charge on the i -th flake. Note that this model is not applicable when the capacitive charge $Q = C_g V_g$ exceeds eN , that is, when all flakes are already charged. Consequently, saturation of the conductivity at high V_g or ϵ is observed (Figure 5b–d).

The $\sigma(V_g)$ dependence predicted by our model (Figure 5d) compares well with measurements on our graphene/hBN FET (Figure 4b), reported for printed devices,^[8] and made on exfoliated graphene/hBN FETs.^[4] For our samples we estimate $E_c = 60$ meV (see Section S4, Supporting Information). We note that this model is applicable to our room temperature measurements, as for our samples the condition $T \ll E_c/k$ is satisfied. The value of activation capacitive charging energy differs from electron hopping activation energy reported for inkjet-printed graphene and graphene oxide.^[39,55] We stress, that in our model we consider only charge transfer between neighboring flakes, while variable range hopping transport is proposed for disordered networks.^[39]

From our experimental $\sigma(V_g)$ dependence, we calculate the carrier field effect mobility to be $\mu_{FE} \approx 25 \text{ cm}^2 (\text{Vs})^{-1}$ and carrier concentration $n < 10^{11} \text{ cm}^{-2}$, comparable to previously reported values for inkjet-printed devices.^[8] Notably, the measured

mobility is significantly lower than typically measured for exfoliated graphene ($\mu > 10\,000\text{ cm}^2\text{ (Vs)}^{-1}$). This difference can be explained within the framework of our model, where the conductivity depends not only on the carrier mobility and density within each graphene flake, but also on the inter-flake charge transfer process. Since our theoretical approach is developed for a low flake packing fraction, the overall conductivity of the printed conducting channel depends strongly on the spatial distribution of individual flakes, which determines the inter-flake tunneling rates, as described by our numerical Monte Carlo simulations (Figure 3). The models developed here provide comprehensive explanation of microscopic tunneling transport (Equation (1)) and macroscopic film conductivity (Equations (2) and (3)). Combining both models for intra- and inter-flake transport in graphene/hBN FETs and Monte-Carlo for disordered 3D-graphene films provides all the necessary tools for modelling carrier transport in 3D-printed graphene heterostructures and field-effect devices. These models explain the observed electrical properties of printed multi-flake graphene structures by accounting for inter-flake charge transfer, hence overcoming the limitations of applying to printed structures models developed only for exfoliated graphene. Our prototype device also demonstrates the potential of graphene inkjet-printing for the scalable fabrication of millimeter-sized Ohmic contacts, thereby overcoming the critical issue of how to reduce contact resistance in emerging 2D electronic materials and technologies.

3. Conclusion

We have used a wide range of characterization techniques, including micro-Raman spectroscopy, TGA, and electrical measurements, to provide detailed structural and functional understanding of inkjet-printed graphene polymers and the effects of annealing on device performance. They show that combining the enhanced deposition qualities of graphene-polymer inks with post-processing to largely remove the polymer, is an effective way to make functional devices based on graphene and other 2D materials. Multi-material vertical stacking of graphene and hBN has successfully demonstrated that printed graphene film acts as an effective charge transport layer. The measured transport characteristics are fully consistent with detailed numerical modeling and shaped by inter-flake electron transitions and extended trajectories that span several printed layers. Inkjet-printed graphene provides high-quality contacts on InSe, exhibiting desired Ohmic behavior. Both theory and experiment indicate that the electrical conductivity of printed graphene films can be improved by increasing the packing fraction of graphene. However, we note that a high packing fraction would lead to strong electrostatic screening effects, which can adversely affect charge carrier mobility and gating action. Understanding the interplay between screening and inter-flake charge transfer is therefore a key challenge for further studies and for developing functional devices based on printed 2D materials. Our results could open diverse applications for inkjet-printed graphene-polymer composites other 2D layers in future multi-material optoelectronic devices.

4. Experimental Section

Materials: The graphene-polymer ink was purchased from Sigma-Aldrich (product number: 793663) and it consisted of liquid exfoliated graphene flakes (average size of 2590 nm^2) encapsulated in ethyl cellulose (EC) dispersed into an 85:15 mixture of cyclohexanone/terpineol to achieve suitable rheological properties for inkjet printing. At a concentration of 2.4 wt% solids, this ink had a density of 9.665 g cm^{-3} , surface tension of 33 mN m^{-1} , and viscosity of 11.3 mPa s at room temperature. The hBN-polymer ink was also purchased from Sigma-Aldrich (product number 901410) with 5.4 wt% EC-hBN composite solids dispersed in the same solvents described above. The AgNP ink was purchased from Advanced Nano Products (product ID: SilverJet DGP-40LT-15C) and consisted of 38.85 wt% of silver nanoparticles dispersed in triethylene glycol monomethyl ether (TGME) and other dispersants.

Inkjet Printing: Graphene ink was deposited on glass or Si/SiO₂ substrate using a drop-on-demand (DoD) piezo driven inkjet printer Fujifilm Dimatix DMP-2800 and a 10 pL drop volume cartridge with nozzles of $a = 21.5\text{ }\mu\text{m}$, $Z = 7.3$. A drop spacing of $20\text{ }\mu\text{m}$ was used. A pause of 30 s between layers was used to allow evaporation of the solvents in order to achieve improved surface morphology and geometrical precision. The films were then annealed for 2 h in a vacuum oven under 1 mbar vacuum at annealing temperatures from 200 to 400 °C. The same process was used for printing hBN films, which were then annealed at 250 °C under 1 mbar vacuum for 30 min. To ensure precise printing geometry, the silver electrodes were printed with $30\text{ }\mu\text{m}$ drop spacing for 1 layer on a heated stage at $90\text{ }^\circ\text{C}^{[43]}$ and then annealed under 1 mbar vacuum for 30 min for curing.

For field effect transistor, a $1800\text{ }\mu\text{m}$ square graphene (5 layers) was first inkjet-printed onto Si/SiO₂ substrate. Two L-shaped silver electrodes ($3000 \times 240\text{ }\mu\text{m}$ bars and $900 \times 750\text{ }\mu\text{m}$ contact pads) were printed using AgNP ink and were used as the source and drain electrodes. The space between the electrodes for the transistor channel was $\approx 100\text{ }\mu\text{m}$. The rectangular insulating layer of hBN ($1300 \times 1800\text{ }\mu\text{m}$) was then printed. Finally, the top gate silver electrode ($900 \times 1500\text{ }\mu\text{m}$) was deposited. Post-deposition, each layer was treated as described above.

Electrical Characterization: To assess the electrical characteristics of the ink, a rectangular line of 5 mm length and $200\text{ }\mu\text{m}$ width was printed on a Si/SiO₂ wafer (monocrystalline Si with SiO₂ thickness on 280 nm). The resistivity measurements were carried out in four-probe geometry with silver electrodes spaced evenly across at least 3 mm length. The measurements were repeated at least three times on different samples. Results are shown as average value and standard deviation. The length and width of lines were measured using an optical microscope. The resistance was measured for five samples for each data point to provide error bars. The measurements were carried out at room temperature and atmospheric pressure.

Compositional and Morphological Characterization: The thermal gravimetric analysis (TGA) of the printed film was characterized using a PerkinElmer TGA 4000 machine, during which the sample was heated from 30 to 500 °C at a heating rate of 10 °C per minute in a nitrogen environment. Scanning electron microscopy images were recorded on Hitachi TM3030 Field Emission SEM.

Raman Spectroscopy: Micro Raman spectroscopy was performed using a Horiba Jobin Yvon LabRAM HR Raman spectrometer equipped with an automated xyz stage (Märzhäuser). To simultaneously scan a range of Raman shifts, a 300 lines mm^{-1} rotatable diffraction grating along a path length of 800 mm was employed. For single point Raman measurements, spectra were acquired using a 532 nm laser (at a power of $0.2\text{ mW }\mu\text{m}^2$, 100× objective) and a confocal pinhole of $200\text{ }\mu\text{m}$ over the range $50\text{--}4000\text{ cm}^{-1}$ with an acquisition time of 120 s and 2 accumulations to improve the signal-to-noise ratio and automatically remove the spikes due to cosmic rays. Raman spectroscopic maps were acquired using a 532 nm laser (at a power of $3.2\text{ }\mu\text{W }\mu\text{m}^2$ conferred using the DuoScan function, 100× objective) and a confocal pinhole of $200\text{ }\mu\text{m}$ over the range $450\text{--}3400\text{ cm}^{-1}$ at $25\text{ }\mu\text{m}$ steps within a square $250 \times 250\text{ }\mu\text{m}$ (a total of 121 spectra per map).

Time-of-Flight Secondary Ion Mass Spectrometry: ToF-SIMS was carried out using a 3D OrbiSIMS (hybrid SIMS) instrument from IONTOF GmbH (Muenster, Germany). Depth profiling data of secondary ion mass spectra were acquired in positive ion polarity mode in dual-beam mode by raster scanning a 30 keV Bi₃⁺ primary ion beam delivering 0.3 pA over regions of 50.6 × 50.6 μm² at the center of a 250×250 μm² sputter crater formed using a 20 keV Ar₂₀₀₀⁺ delivering 5 nA. A low-energy (20 eV) electron flood gun was employed to neutralize charge build up. The ToF analyzer was set with a 200 μs cycle time, resulting in a mass range between 0 and 2232 mass units. The simsMVA software^[56] was used to correct 3D distribution of secondary ions and produce 3D rendered visualizations.

Cross-Section Imaging: A cross-section of the FET sample was exposed by focused ion beam (FIB-SEM) using an FEI Quanta200 3D Dual Beam FIB-SEM operated with a Ga⁺ beam. High resolution micrographs of the cross section were obtained with a JEOL 7100F FEG-SEM instrument, which uses an in-lens Schottky field emission source. The microscope was operated with a 5 keV electron beam and at a working distance of 10 mm.

Supporting Information

Supporting Information is available from the Wiley Online Library or from the author.

Acknowledgements

F.W. and J.H.G. contributed equally to this work. This work was funded by the Engineering and Physical Sciences Research Council Programme Grant [grant number EP/P031684/1] and the Dstl. The authors acknowledge access to the facilities at the Nanoscale and Microscale Research Centre (nmRC) at the University of Nottingham, Strategic Equipment Grant [grant number EP/P029868/1] and technical support from Dr. Christopher D. J. Parmenter, Mr. Martin Roe, and Dr. David Scurr.

Conflict of Interest

The authors declare no conflict of interest.

Keywords

field effect transistors, graphene, inkjet printing, Monte Carlo simulations, percolation dynamics

Received: September 1, 2020

Revised: October 8, 2020

Published online:

- [1] A. H. C. Neto, F. Guinea, N. M. R. Peres, K. S. Novoselov, A. K. Geim, *Rev. Mod. Phys.* **2009**, *81*, 109.
- [2] H. C. Lee, W.-W. Liu, S.-P. Chai, A. R. Mohamed, A. Aziz, C.-S. Khe, N. M. S. Hidayah, U. Hashim, *RSC Adv.* **2017**, *7*, 15644.
- [3] C. Backes, A. M. Abdelkader, C. Alonso, A. Andrieux-Ledier, R. Arenal, J. Azpeitia, N. Balakrishnan, L. Banszerus, J. Barjon, R. Bartali, S. Bellani, C. Berger, R. Berger, M. M. B. Ortega, C. Bernard, P. H. Beton, A. Beyer, A. Bianco, P. Bøggild, F. Bonaccorso, G. B. Barin, C. Botas, R. A. Bueno,

- D. Carriazo, A. Castellanos-Gomez, M. Christian, A. Ciesielski, T. Ciuk, M. T. Cole, J. Coleman, et al, *2D Mater.* **2020**, *7*, 022001.
- [4] S. V. Morozov, K. S. Novoselov, M. I. Katsnelson, F. Schedin, D. C. Elias, J. A. Jaszczak, A. K. Geim, *Phys. Rev. Lett.* **2008**, *100*, 016602.
- [5] J. N. Coleman, M. Lotya, A. O'Neill, S. D. Bergin, P. J. King, U. Khan, K. Young, A. Gaucher, S. De, R. J. Smith, I. V. Shvets, S. K. Arora, G. Stanton, H.-Y. Kim, K. Lee, G. T. Kim, G. S. Duesberg, T. Hallam, J. J. Boland, J. J. Wang, J. F. Donegan, J. C. Grunlan, G. Moriarty, A. Shmeliov, R. J. Nicholls, J. M. Perkins, E. M. Grieveson, K. Theuwissen, D. W. McComb, P. D. Nellist, et al, *Science* **2011**, *331*, 568.
- [6] J. N. Coleman, *Acc. Chem. Res.* **2013**, *46*, 14.
- [7] E. Jabari, F. Ahmed, F. Liravi, E. B. Secor, L. Lin, E. Toyserkani, *2D Mater.* **2019**, *6*, 042004.
- [8] T. Carey, S. Cacovich, G. Divitini, J. Ren, A. Mansouri, J. M. Kim, C. Wang, C. Ducati, R. Sordan, F. Torrisi, *Nat. Commun.* **2017**, *8*, 1.
- [9] D. Vernardou, K. C. Vasilopoulos, G. Kenanakis, *Appl. Phys. A* **2017**, *123*, 623.
- [10] R. M. Hensleigh, H. Cui, J. S. Oakdale, J. C. Ye, P. G. Campbell, E. B. Duoss, C. M. Spadaccini, X. Zheng, M. A. Worsley, *Mater. Horiz.* **2018**, *5*, 1035.
- [11] R. D. Farahani, M. Dubé, D. Therriault, *Adv. Mater.* **2016**, *28*, 5794.
- [12] H. Guo, R. Lv, S. Bai, *Nano Mater. Sci.* **2019**, *1*, 101.
- [13] Y. S. Rim, S.-H. Bae, H. Chen, N. De Marco, Y. Yang, *Adv. Mater.* **2016**, *28*, 4415.
- [14] N. Huo, G. Konstantatos, *Adv. Mater.* **2018**, *30*, 1801164.
- [15] B. Davaji, H. D. Cho, M. Malakoutian, J.-K. Lee, G. Panin, T. W. Kang, C. H. Lee, *Sci. Rep.* **2017**, *7*, 1.
- [16] R. Worsley, L. Pimpolari, D. McManus, N. Ge, R. Ionescu, J. A. Wittkopf, A. Alieva, G. Basso, M. Macucci, G. Iannaccone, K. S. Novoselov, H. Holder, G. Fiori, C. Casiraghi, *ACS Nano* **2019**, *13*, 54.
- [17] K. Rajan, E. Garofalo, A. Chiolerio, *Sensors* **2018**, *18*, 367.
- [18] B. Wang, A. Facchetti, *Adv. Mater.* **2019**, *31*, 1901408.
- [19] E. B. Secor, *Phys. Chem. Lett.* **2013**, *4*, 1347.
- [20] R. M. Hill, *Proc. R. Soc. A* **1969**, *309*, 377.
- [21] C. J. Adkins, J. D. Benjamin, J. M. D. Thomas, J. W. Gardner, A. J. McGeown, *J. Phys. C: Solid State Phys.* **1984**, *17*, 4633.
- [22] A. C. Ferrari, D. M. Basko, *Nat. Nanotechnol.* **2013**, *8*, 235.
- [23] A. C. Ferrari, J. Robertson, *Phys. Rev. B* **2000**, *61*, 14095.
- [24] S. Santangelo, G. Messina, G. Faggio, M. Lanza, C. Milone, *J. Raman Spectrosc.* **2011**, *42*, 593.
- [25] J.-B. Wu, M.-L. Lin, X. Cong, H.-N. Liua, P.-H. Tan, *Chem. Soc. Rev.* **2018**, *47*, 1822.
- [26] A. C. Ferrari, J. C. Meyer, V. Scardaci, C. Casiraghi, M. Lazzeri, F. Mauri, S. Piscanec, D. Jiang, K. S. Novoselov, S. Roth, A. K. Geim, *Phys. Rev. Lett.* **2006**, *97*, 187401.
- [27] L. M. Malard, M. A. Pimenta, G. Dresselhaus, M. S. Dresselhaus, *Phys. Rep.* **2009**, *473*, 51.
- [28] E. Jabari, E. Toyserkani, *J. Phys. D: Appl. Phys.* **2015**, *48*, 375503.
- [29] X. G. Li, M. R. Huang, H. Bai, *J. Appl. Polym. Sci.* **1999**, *73*, 2927.
- [30] S. Santra, G. Hu, R. C. T. Howe, A. De Luca, S. Z. Ali, F. Udrea, J. W. Gardner, S. K. Ray, P. K. Guha, T. Hasan, *Sci. Rep.* **2015**, *5*, 17374.
- [31] S. De, P. J. King, P. E. Lyons, U. Khan, J. N. Coleman, *ACS Nano* **2010**, *4*, 7064.
- [32] E. B. Secor, P. L. Prabhuramirashi, K. Puntambekar, M. L. Geier, M. C. Hersam, *J. Phys. Chem. Lett.* **2013**, *4*, 1347.
- [33] D. S. Schulman, A. J. Arnold, S. Das, *Chem. Soc. Rev.* **2018**, *47*, 3037.
- [34] Y. Xu, C. Cheng, S. Du, J. Yang, B. Yu, J. Luo, W. Yin, E. Li, S. Dong, P. Ye, X. Duan, *ACS Nano* **2016**, *10*, 4895.
- [35] Y.-T. Lin, X.-Q. Zhang, P.-H. Chen, C.-C. Chi, E.-C. Lin, J.-G. Rong, C. Ouyang, Y.-F. Chen, Y.-H. Lee, *Nanoscale* **2020**, *15*, 1.
- [36] D. A. Bandurin, A. V. Tyurnina, G. L. Yu, A. Mishchenko, V. Zólyomi, S. V. Morozov, R. K. Kumar, R. V. Gorbachev, Z. R. Kudrynskiy,

- S. Pezzini, Z. D. Kovalyuk, U. Zeitler, K. S. Novoselov, A. Patanè, L. Eaves, I. V. Grigorieva, V. I. Fal'ko, A. K. Geim, Y. Cao, *Nat. Nanotechnol.* **2017**, *12*, 223.
- [37] G. W. Mudd, S. A. Svatek, L. Hague, O. Makarovskiy, Z. R. Kudrynskiy, C. J. Mellor, P. H. Beton, L. Eaves, K. S. Novoselov, Z. D. Kovalyuk, E. E. Vdovin, A. J. Marsden, N. R. Wilson, A. Patanè, *Adv. Mater.* **2015**, *27*, 3760.
- [38] I. Mintyanskiy, P. Savitskiy, Z. Kovalyuk, *Phys. Status Solidi* **2015**, *252*, 346.
- [39] B. Muchharla, T. N. Narayanan, K. Balakrishnan, P. M. Ajayan, S. Talapatra, *2D Mater.* **2014**, *1*, 011008.
- [40] D. Kong, L. T. Le, Y. Li, J. L. Zunino, W. Lee, *Langmuir* **2012**, *28*, 13467.
- [41] H. Seo, S. Ahn, J. Kim, Y.-A. Lee, K.-H. Chung, K.-J. Jeon, *Sci. Rep.* **2015**, *4*, 5642.
- [42] A. Bellunato, S. D. Vrbica, C. Sabater, E. W. de Vos, R. Fermin, K. N. Kanneworff, F. Galli, J. M. van Ruitenbeek, G. F. Schneider, *Nano Lett.* **2018**, *18*, 2505.
- [43] J. G. Simmons, *J. Appl. Phys.* **1963**, *34*, 1793.
- [44] M. Büttiker, Y. Imry, R. Landauer, S. Pinhas, *Phys. Rev. B* **1985**, *31*, 6207.
- [45] J. Greensite, *An Introduction to Quantum Theory*, IOP Publishing, Bristol **2017**.
- [46] C. S. Lau, J. A. Mol, J. H. Warner, G. A. D. Briggs, *Phys. Chem. Chem. Phys.* **2014**, *16*, 20398.
- [47] K. Ullmann, P. B. Coto, S. Leitherer, A. Molina-Ontoria, N. Martín, M. Thoss, H. B. Weber, *Nano Lett.* **2015**, *15*, 3512.
- [48] A. Behnam, A. Ural, *Phys. Rev. B* **2007**, *75*, 125432.
- [49] J. Hicks, A. Behnam, A. Ural, *Appl. Phys. Lett.* **2009**, *95*, 213103.
- [50] I. V. Vodolazskaya, A. V. Eserkepov, R. K. Akhuzhanov, Y. Yu, Tarasevich, *J. Appl. Phys.* **2019**, *126*, 244903.
- [51] X.-Y. Fang, X.-X. Yu, H.-M. Zheng, H.-B. Jin, L. Wang, M.-S. Cao, *Phys. Lett. A* **2015**, *379*, 2245.
- [52] E. Saleh, F. Zhang, Y. He, J. Vaithilingam, J. L. Fernandez, R. Wildman, I. Ashcroft, R. Hague, P. Dickens, C. Tuck, *Adv. Mater. Technol.* **2017**, *2*, 1700134.
- [53] L. Britnell, R. V. Gorbachev, A. K. Geim, L. A. Ponomarenko, A. Mishchenko, M. T. Greenaway, T. M. Fromhold, K. S. Novoselov, L. Eaves, *Nat. Commun.* **2013**, *4*, 1794.
- [54] C. Stampfer, E. Schurtenberger, F. Molitor, J. Güttinger, T. Ihn, K. Ensslin, *Nano Lett.* **2008**, *8*, 2378.
- [55] I. Banerjee, T. Faris, Z. Stoeva, P. G. Harris, J. Chen, A. K. Sharma, A. K. Ray, *2D Mater.* **2017**, *4*, 015036.
- [56] G. F. Trindada, M.-L. Abel, J. F. Watts, *Chemom. Intell. Lab. Syst.* **2018**, *182*, 180.